Supplemental Material for:
Strong parametric coupling between two ultra-coherent membrane modes

David Hälg,[1] Thomas Gisler,[1] Eric C. Langman,[2,3] Shobhna Misra,[1] Oded Zilberberg,[4,5] Albert Schliesser,[2,3] Christian L. Degen,[1,6] and Alexander Eichler[1,*]

[1] *Laboratory for Solid State Physics, ETH Zürich, 8093 Zürich, Switzerland.*
[2] *Niels Bohr Institute, University of Copenhagen, 2100 Copenhagen, Denmark.*
[3] *Center for Hybrid Quantum Networks, Niels Bohr Institute, University of Copenhagen, 2100 Copenhagen, Denmark.*
[4] *Institute for Theoretical Physics, ETH Zürich, 8093 Zürich, Switzerland.*
[5] *Department of Physics, University of Konstanz, D-78457 Konstanz, Germany.*
[6] *Quantum Center, ETH Zurich, 8093 Zurich, Switzerland.*

S1. CHARGE INVESTIGATIONS

In Fig. S1, we show the amplitude of the antisymmetric mode while scanning over the surface with a constant photon pressure (laser) drive and with a constant tip voltage drive. For the laser drive, we observe a constant amplitude, while the electrically driven amplitude varies significantly. This result is in agreement with our assumption that inhomogeneous surface charges ('voltage patches') are responsible for the electrical interaction of the membrane resonator with the scanning tip. Further systematic studies will hopefully allow us to quantify the charge distribution and to identify potential microscopic origins of the phenomenon. We speculate that such inhomogeneous charge distributions could contribute towards the linear and nonlinear damping of the resonators, as well as to frequency fluctuations [1, 2].

S2. SECOND DEVICE DATA

We repeated the experiment shown in Fig. 4 with a second device with $Q_A = 33 \times 10^6$ and $Q_S = 31 \times 10^6$. The steady-state amplitudes were recorded at the position (0/0) of Fig. S1(b) and at a distance of 100 nm. At this position,

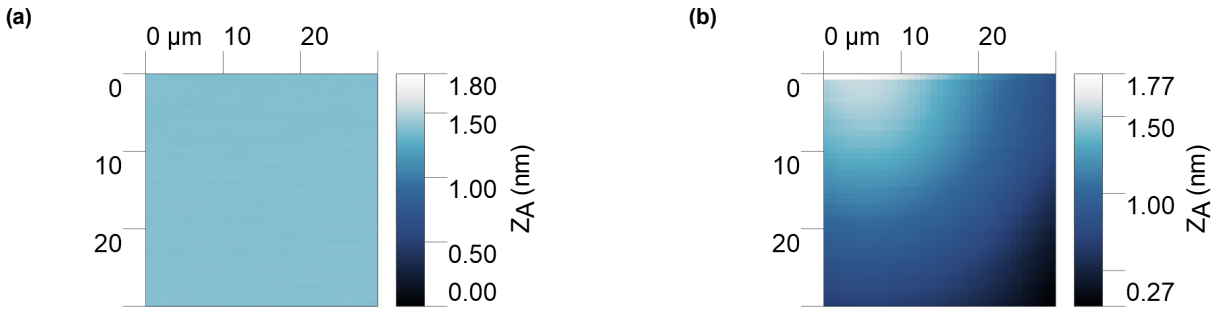

FIG. S1. **Surface charge imaging.** Tip scanned over the surface with (a) a laser drive and (b) a tip drive. This data was recorded with a second device at a distance of 1.3 µm.

* Corresponding author: eichlera@ethz.ch

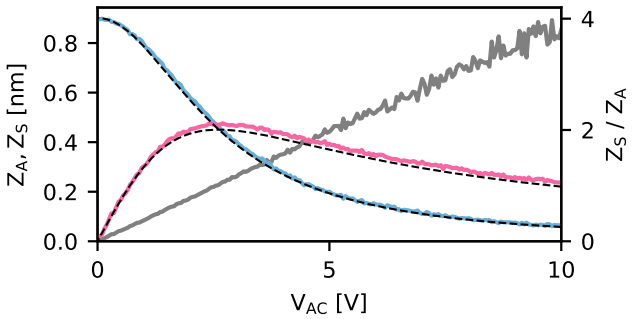

FIG. S2. **Steady-state amplitudes.** Mode amplitudes as a function of V_{AC} with a constant photon pressure drive at $f_d = f_A$ and parametric pumping at f_Δ at a distance d =100 nm (left axis). Blue and pink: measured amplitude of the anti-symmetric and symmetric mode, respectively. Black dashed lines: solutions of Eq. (2) for $\dot{u}_{S,A} = \dot{v}_{S,A} = 0$. Grey: Z_S/Z_A extracted from the measurements (right axis). This data was recorded with a second device.

we find $g = 0.245\,\mathrm{rad\,s^{-1}}$ for $V_{\mathrm{AC}} = 10\,\mathrm{V}$, which is roughly five times smaller than the coupling measured for the device in the main text under similar conditions.

S3. SLOW-FLOW DERIVATION

We can model our system as two parametrically coupled, linear oscillators

$$\ddot{z}_A + \Gamma_A \dot{z}_A + \omega_A^2 z_A - J z_S = F_A/m_A \tag{S1}$$

$$\ddot{z}_S + \Gamma_S \dot{z}_S + \omega_S^2 z_S - J z_A = F_S/m_S\,. \tag{S2}$$

with driving frequency Ω, coupling $J = \lambda\cos(\Omega t)$, dissipation Γ, displacements z_A, z_S, angular rotation frequencies ω_1, ω_2, forces F_A, F_S, and masses m_A, m_S. We can set the force terms 0 for the moment, and insert them later if needed. Alternatively it could also be simulated.[3]

We can split these equations of motion into two first order equations with $z_i = q_j$, $\dot{z}_i = p_j$, $i \in \{A, S\}$ and $j \in \{1, 2\}$,

$$\dot{q}_1 = p_1\,, \tag{S3}$$

$$\dot{p}_1 = -\omega_1^2 q_1 + \lambda\cos(\Omega t) q_2 - \Gamma p_1\,, \tag{S4}$$

$$\dot{q}_2 = p_2\,, \tag{S5}$$

$$\dot{p}_2 = -\omega_2^2 q_2 + \lambda\cos(\Omega t) q_1 - \Gamma p_2\,. \tag{S6}$$

We change here from $\{A, S\}$ to $\{1, 2\}$ for nicer looking equations, but the indices have nothing to do with the defect site labels 1 and 2. We then move to a rotating frame at an angular frequency Ω_1 for Eqs. (S3) and (S4) and at Ω_2 for Eqs. (S5) and (S6) using van der Pol transformations [4]. By integrating the transformed equations over one period, i.e. over $2\pi/\Omega_1$ and $2\pi/\Omega_2$ respectively, we arrive at the equation

$$\begin{pmatrix} \dot{u}_1 \\ \dot{v}_1 \\ \dot{u}_2 \\ \dot{v}_2 \end{pmatrix} = \mathbf{P} \begin{pmatrix} u_1 \\ v_1 \\ u_2 \\ v_2 \end{pmatrix} = \begin{pmatrix} -\frac{\Gamma}{2} & a_{12} & a_{13} & a_{14} \\ a_{21} & -\frac{\Gamma}{2} & a_{23} & a_{24} \\ a_{31} & a_{32} & -\frac{\Gamma}{2} & a_{34} \\ a_{41} & a_{42} & a_{43} & -\frac{\Gamma}{2} \end{pmatrix} \begin{pmatrix} u_1 \\ v_1 \\ u_2 \\ v_2 \end{pmatrix} \tag{S7}$$

for the slow-flow coordinates u_i and v_i, i.e., the in-phase and out-of-phase oscillation amplitudes. The matrix elements of $\mathbf{P}$ are

$$a_{12} = -\,a_{21} = \frac{\Omega_1}{2\pi}\left(\pi - \frac{\pi\omega_1^2}{\Omega_1^2}\right), \tag{S8}$$

$$a_{34} = -\,a_{43} = \frac{\Omega_2}{2\pi}\left(\pi - \frac{\pi\omega_2^2}{\Omega_2^2}\right), \tag{S9}$$

$$\begin{aligned} a_{13} =& \lambda\Omega_1 \left(\frac{2\left(\Omega^2 - \Omega_1^2 + \Omega_2^2\right) - (\Omega - \Omega_1 + \Omega_2)(\Omega + \Omega_1 + \Omega_2)\cos\left(\frac{2\pi(\Omega-\Omega_2)}{\Omega_1}\right)}{4\pi(\Omega - \Omega_1 - \Omega_2)(\Omega + \Omega_1 - \Omega_2)(\Omega - \Omega_1 + \Omega_2)(\Omega + \Omega_1 + \Omega_2)} \right. \\ & \left. - \frac{(\Omega - \Omega_1 - \Omega_2)\cos\left(\frac{2\pi(\Omega+\Omega_2)}{\Omega_1}\right)}{4\pi(\Omega - \Omega_1 - \Omega_2)(\Omega - \Omega_1 + \Omega_2)(\Omega + \Omega_1 + \Omega_2)} \right), \end{aligned} \tag{S10}$$

$$a_{14} = \frac{\lambda\Omega_1 \left(\frac{\sin\left(\frac{2\pi(\Omega+\Omega_2)}{\Omega_1}\right)}{(\Omega-\Omega_1+\Omega_2)(\Omega+\Omega_1+\Omega_2)} - \frac{\sin\left(\frac{2\pi(\Omega-\Omega_2)}{\Omega_1}\right)}{\Omega^2 - 2\Omega\Omega_2 - \Omega_1^2 + \Omega_2^2} \right)}{4\pi}, \tag{S11}$$

$$a_{23} = \frac{\lambda \left(\frac{(\Omega-\Omega_2)\sin\left(\frac{2\pi(\Omega-\Omega_2)}{\Omega_1}\right)}{(\Omega+\Omega_1-\Omega_2)(-\Omega+\Omega_1+\Omega_2)} - \frac{(\Omega+\Omega_2)\sin\left(\frac{2\pi(\Omega+\Omega_2)}{\Omega_1}\right)}{(\Omega-\Omega_1+\Omega_2)(\Omega+\Omega_1+\Omega_2)} \right)}{4\pi}, \tag{S12}$$

$$\begin{aligned} a_{24} =& \lambda \left(\frac{-2\Omega_2\left(\Omega^2 + \Omega_1^2 - \Omega_2^2\right) + (\Omega - \Omega_2)(\Omega - \Omega_1 + \Omega_2)(\Omega + \Omega_1 + \Omega_2)\cos\left(\frac{2\pi(\Omega-\Omega_2)}{\Omega_1}\right)}{4\pi(-\Omega + \Omega_1 - \Omega_2)(\Omega + \Omega_1 - \Omega_2)(-\Omega + \Omega_1 + \Omega_2)(\Omega + \Omega_1 + \Omega_2)} \right. \\ & \left. - \frac{(\Omega + \Omega_2)(\Omega - \Omega_1 - \Omega_2)\cos\left(\frac{2\pi(\Omega+\Omega_2)}{\Omega_1}\right)}{4\pi(-\Omega + \Omega_1 - \Omega_2)(-\Omega + \Omega_1 + \Omega_2)(\Omega + \Omega_1 + \Omega_2)} \right), \end{aligned} \tag{S13}$$

$$\begin{aligned} a_{31} =& \lambda\Omega_2 \left(\frac{2\left(\Omega^2 + \Omega_1^2 - \Omega_2^2\right) - (\Omega + \Omega_1 - \Omega_2)(\Omega + \Omega_1 + \Omega_2)\cos\left(\frac{2\pi(\Omega-\Omega_1)}{\Omega_2}\right)}{4\pi(\Omega - \Omega_1 - \Omega_2)(\Omega + \Omega_1 - \Omega_2)(\Omega - \Omega_1 + \Omega_2)(\Omega + \Omega_1 + \Omega_2)} \right. \\ & \left. - \frac{(\Omega - \Omega_1 - \Omega_2)\cos\left(\frac{2\pi(\Omega+\Omega_1)}{\Omega_2}\right)}{4\pi(\Omega - \Omega_1 - \Omega_2)(\Omega + \Omega_1 - \Omega_2)(\Omega + \Omega_1 + \Omega_2)} \right), \end{aligned} \tag{S14}$$

$$a_{32} = \frac{\lambda\Omega_2 \left(\frac{\sin\left(\frac{2\pi(\Omega+\Omega_1)}{\Omega_2}\right)}{(\Omega+\Omega_1-\Omega_2)(\Omega+\Omega_1+\Omega_2)} - \frac{\sin\left(\frac{2\pi(\Omega-\Omega_1)}{\Omega_2}\right)}{(\Omega-\Omega_1)^2 - \Omega_2^2} \right)}{4\pi}, \tag{S15}$$

$$\tag{S16}$$

$$a_{41} = \frac{\lambda\left(\frac{(\Omega_1-\Omega)\sin\left(\frac{2\pi(\Omega-\Omega_1)}{\Omega_2}\right)}{(\Omega-\Omega_1)^2-\Omega_2^2} - \frac{(\Omega+\Omega_1)\sin\left(\frac{2\pi(\Omega+\Omega_1)}{\Omega_2}\right)}{(\Omega+\Omega_1-\Omega_2)(\Omega+\Omega_1+\Omega_2)}\right)}{4\pi}, \tag{S17}$$

$$a_{42} = -\lambda\left(\frac{-2\Omega_1\left(\Omega^2-\Omega_1^2+\Omega_2^2\right)+(\Omega-\Omega_1)(\Omega+\Omega_1-\Omega_2)(\Omega+\Omega_1+\Omega_2)\cos\left(\frac{2\pi(\Omega-\Omega_1)}{\Omega_2}\right)}{4\pi(\Omega+\Omega_1-\Omega_2)(\Omega-\Omega_1+\Omega_2)(-\Omega+\Omega_1+\Omega_2)(\Omega+\Omega_1+\Omega_2)}\right.$$
$$\left. -\frac{(\Omega+\Omega_1)(\Omega-\Omega_1-\Omega_2)\cos\left(\frac{2\pi(\Omega+\Omega_1)}{\Omega_2}\right)}{4\pi(\Omega+\Omega_1-\Omega_2)(-\Omega+\Omega_1+\Omega_2)(\Omega+\Omega_1+\Omega_2)}\right). \tag{S18}$$

Looking at the off-diagonal 2×2 blocks in P that are responsible for mode coupling, we see that the coupling coefficients are time dependent for most choices of Ω_1 and Ω_2. In our frame rotating at the resonance frequencies of the two modes of interest, a coupling coefficient that varies over time averages out over long enough observation periods and does not contribute significantly. A time-independent, strong coupling can be achieved for $\Omega = \pm(\Omega_1 \pm \Omega_2)$. We will therefore only consider the cases of driving at the frequency difference and at the frequency sum.

A. parametric coupling at $\Omega = \Omega_1 - \Omega_2$

For $\Omega = \Omega_1 - \Omega_2$ the propagator takes the form

$$\begin{pmatrix}
-\frac{\Gamma}{2} & \frac{\Omega_1^2-\omega_1^2}{2\Omega_1} & -\frac{\lambda\Omega_1\sin^2\left(\frac{2\pi\Omega_2}{\Omega_1}\right)}{8\pi\Omega_2(\Omega_1-\Omega_2)} & \frac{\lambda}{4\Omega_1}-\frac{\lambda\Omega_1\sin\left(\frac{4\pi\Omega_2}{\Omega_1}\right)}{16\pi\Omega_2(\Omega_1-\Omega_2)} \\
\frac{(\omega_1-\Omega_1)(\omega_1+\Omega_1)}{2\Omega_1} & -\frac{\Gamma}{2} & \frac{1}{16}\lambda\left(-\frac{(\Omega_1-2\Omega_2)\sin\left(\frac{4\pi\Omega_2}{\Omega_1}\right)}{\pi\Omega_2(\Omega_1-\Omega_2)}-\frac{4}{\Omega_1}\right) & \frac{\lambda(\Omega_1-2\Omega_2)\sin^2\left(\frac{2\pi\Omega_2}{\Omega_1}\right)}{8\pi\Omega_2(\Omega_1-\Omega_2)} \\
\frac{\lambda\Omega_2\sin^2\left(\frac{2\pi\Omega_1}{\Omega_2}\right)}{8\pi\Omega_1(\Omega_1-\Omega_2)} & \frac{\lambda\left(\frac{\Omega_2^2\sin\left(\frac{4\pi\Omega_1}{\Omega_2}\right)}{\pi\Omega_1^2-\pi\Omega_1\Omega_2}+4\right)}{16\Omega_2} & -\frac{\Gamma}{2} & \frac{\Omega_2^2-\omega_2^2}{2\Omega_2} \\
\frac{1}{16}\lambda\left(\frac{(\Omega_2-2\Omega_1)\sin\left(\frac{4\pi\Omega_1}{\Omega_2}\right)}{\pi\Omega_1(\Omega_1-\Omega_2)}-\frac{4}{\Omega_2}\right) & \frac{\lambda(2\Omega_1-\Omega_2)\sin^2\left(\frac{2\pi\Omega_1}{\Omega_2}\right)}{8\pi\Omega_1(\Omega_1-\Omega_2)} & \frac{(\omega_2-\Omega_2)(\omega_2+\Omega_2)}{2\Omega_2} & -\frac{\Gamma}{2}
\end{pmatrix}. \tag{S19}$$

The trigonometric terms with Ω_1/Ω_2 and Ω_2/Ω_1 lead to micro-motion, but we assume the rotating pictures to be sufficiently close to one another, i.e., $\Omega_1/\Omega_2 = \Omega_2/\Omega_1 = 1$. With this approximation, we arrive at

$$\mathbf{P} = \begin{pmatrix}
-\frac{\Gamma}{2} & \frac{\Omega_1}{2}-\frac{\omega_1^2}{2\Omega_1} & 0 & \frac{\lambda}{4\Omega_1} \\
\frac{\omega_1^2}{2\Omega_1}-\frac{\Omega_1}{2} & -\frac{\Gamma}{2} & -\frac{\lambda}{4\Omega_1} & 0 \\
0 & \frac{\lambda}{4\Omega_2} & -\frac{\Gamma}{2} & \frac{\Omega_2}{2}-\frac{\omega_2^2}{2\Omega_2} \\
-\frac{\lambda}{4\Omega_2} & 0 & \frac{\omega_2^2}{2\Omega_2}-\frac{\Omega_2}{2} & -\frac{\Gamma}{2}
\end{pmatrix}. \tag{S20}$$

To simplify the notation, we define $\delta_1 = \Omega_1 - \omega_1$, $\delta_2 = \Omega_2 - \omega_2$, $\omega_0 = \frac{1}{2}(\omega_1+\omega_2)$ and $\lambda = 2\omega_0 g$. For small detunings, we can set $\frac{\Omega_1}{\omega_1} \approx 1$ and $\frac{\Omega_2}{\omega_2} \approx 1$ and reach the result of equation (2) of the main manuscript

$$\mathbf{P} = \begin{pmatrix} -\frac{\Gamma}{2} & \delta_1\omega_0 & 0 & \frac{g}{2} \\ -\delta_1\omega_0 & -\frac{\Gamma}{2} & -\frac{g}{2} & 0 \\ 0 & \frac{g}{2} & -\frac{\Gamma}{2} & \delta_2\omega_0 \\ -\frac{g}{2} & 0 & -\delta_2\omega_0 & -\frac{\Gamma}{2} \end{pmatrix}. \tag{S21}$$

The only difference is that we labeled the symmetric (antisymmetric) mode with S (A) instead of 1 (2).

B. parametric coupling at $\Omega = \Omega_1 + \Omega_2$

At $\Omega = \Omega_1 + \Omega_2$ the propagator takes the form

$$\begin{pmatrix} -\frac{\Gamma}{2} & \frac{\Omega_1^2-\omega_1^2}{2\Omega_1} & \frac{\lambda\Omega_1 \sin^2\left(\frac{2\pi\Omega_2}{\Omega_1}\right)}{8\pi\Omega_2(\Omega_1+\Omega_2)} & \frac{\lambda\left(\frac{\Omega_1^2 \sin\left(\frac{4\pi\Omega_2}{\Omega_1}\right)}{\pi\Omega_1\Omega_2+\pi\Omega_2^2}-4\right)}{16\Omega_1} \\ \frac{(\omega_1-\Omega_1)(\omega_1+\Omega_1)}{2\Omega_1} & -\frac{\Gamma}{2} & \frac{1}{16}\lambda\left(-\frac{(\Omega_1+2\Omega_2)\sin\left(\frac{4\pi\Omega_2}{\Omega_1}\right)}{\pi\Omega_2(\Omega_1+\Omega_2)}-\frac{4}{\Omega_1}\right) & \frac{\lambda(\Omega_1+2\Omega_2)\sin^2\left(\frac{2\pi\Omega_2}{\Omega_1}\right)}{8\pi\Omega_2(\Omega_1+\Omega_2)} \\ \frac{\lambda\Omega_2 \sin^2\left(\frac{2\pi\Omega_1}{\Omega_2}\right)}{8\pi\Omega_1(\Omega_1+\Omega_2)} & \frac{\lambda\left(\frac{\Omega_2^2 \sin\left(\frac{4\pi\Omega_1}{\Omega_2}\right)}{\pi\Omega_1^2+\pi\Omega_1\Omega_2}-4\right)}{16\Omega_2} & -\frac{\Gamma}{2} & \frac{\Omega_2^2-\omega_2^2}{2\Omega_2} \\ \frac{1}{16}\lambda\left(-\frac{(2\Omega_1+\Omega_2)\sin\left(\frac{4\pi\Omega_1}{\Omega_2}\right)}{\pi\Omega_1(\Omega_1+\Omega_2)}-\frac{4}{\Omega_2}\right) & \frac{\lambda(2\Omega_1+\Omega_2)\sin^2\left(\frac{2\pi\Omega_1}{\Omega_2}\right)}{8\pi\Omega_1(\Omega_1+\Omega_2)} & \frac{(\omega_2-\Omega_2)(\omega_2+\Omega_2)}{2\Omega_2} & -\frac{\Gamma}{2} \end{pmatrix} \tag{S22}$$

Using a similar set of assumption as in the previous case, we obtain

$$\mathbf{P} = \begin{pmatrix} -\frac{\Gamma}{2} & \delta_1\omega_0 & 0 & -\frac{g}{2} \\ -\delta_1\omega_0 & -\frac{\Gamma}{2} & -\frac{g}{2} & 0 \\ 0 & -\frac{g}{2} & -\frac{\Gamma}{2} & \delta_2\omega_0 \\ -\frac{g}{2} & 0 & -\delta_2\omega_0 & -\frac{\Gamma}{2}\,. \end{pmatrix} \tag{S23}$$

S4. DERIVATION OF EQ. (4) AND (5)

For the experiment presented in Fig. 4, the phases of both modes are depend on the external force. Equations (4) and (5) can be derived as follows: an external force F_A drives the symmetric mode to the standard linear response

$$Z_A = \frac{F_A}{m\omega_0\Gamma} e^{-\frac{\pi}{2}} = -i\frac{F_A}{m\omega_0\Gamma}\,. \tag{S24}$$

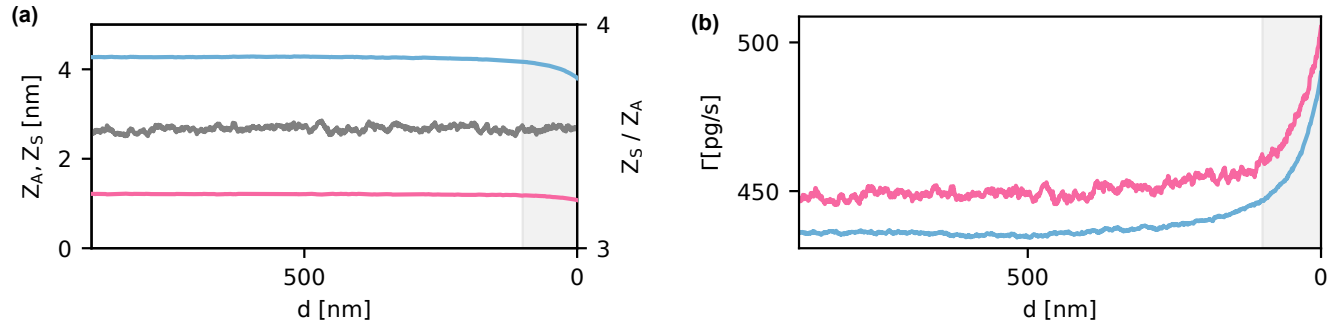

FIG. S3. **Non-contact friction.** (a) Mode amplitudes as a function of distance d with laser driving on both modes. Blue and pink: measured amplitude of the anti-symmetric and symmetric mode, respectively. Grey: ratio of the modes (right axis). (b) Change in dissipation $\Gamma = m\omega/Q$ due to non-contact friction. Blue and pink: measured dissipation of the anti-symmetric and symmetric mode, respectively. Shaded grey: region where d <100 nm.

Adding a coupling term Jz_A with the component $g\omega_0 Z_A \cos(\omega_S t)$ acting resonantly on Z_S, we obtain via the same mechanism

$$Z_S = \frac{gZ_A}{\Gamma} e^{-\frac{\pi}{2}} = -i\frac{gZ_A}{\Gamma}\,, \tag{S25}$$

which we divide by Z_A to obtain Eq. (5). Z_S exerts a coupling force $g\omega_0 Z_S$ back on z_A. The steady-state equation we find for Z_A is

$$Z_A = -i\frac{F_A}{m\omega_0\Gamma} - i\frac{gZ_S}{\Gamma} = -i\frac{F_A}{m\omega_0\Gamma} - \left(\frac{g}{\Gamma}\right)^2 Z_A\,, \tag{S26}$$

which we solve for Z_A to obtain Eq. (4).

S5. NON-CONTACT FRICTION

In Fig. S3 (a) we present measurements of the tip-membrane non-contact friction. We drive both modes at their individual resonance frequencies with the laser modulation technique and record their response amplitudes as a function of the tip-surface separation d. In the plot, we can see that the amplitude decreases only for small distances for both modes and that their ratio remains constant. The extracted non-contact friction as a function of d is plotted in Fig. S3(b). Since it contributes less than 10 % to the membrane's total friction up to $d < 10$ nm, we neglect this additional dissipation channel in the following.

S6. MICROSCOPIC MODEL FOR TIP-SURFACE INTERACTION

In order to shed light onto the microscopic origin of the parametric drive, we start from a very simple model. We assume that a single charge q_{surf} is located on the membrane surface at a tip-surface distance d and at a radial displacement r, see Fig. S4(a). This charge experiences an electric force in z-direction, $F_{\mathrm{el}} = E_z(d,r)q_{\mathrm{surf}}$, in response to the z-component of the electrical tip field at the charge's location, $E_z(d,r) = \frac{\partial V_{\mathrm{tip}}}{\partial z}$. For convenience, we will drop

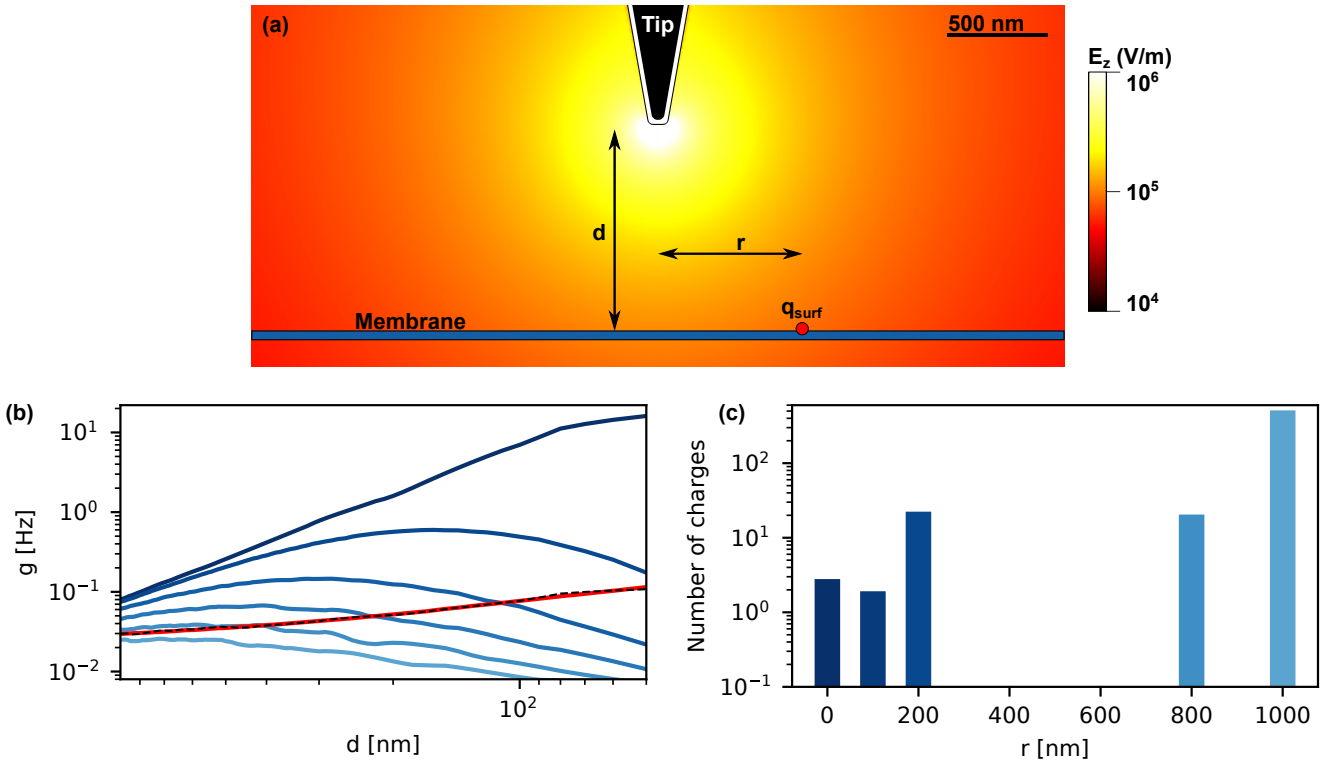

FIG. S4. **Charge model.** (a) Sketch of the microscopic model. The background coloring shows the electric field in z-direction, E_z, as simulated in COMSOL. A charge q_{surf} is at a radial distance r and a z-distance d from the tip. The platinum layer (white) around the silicon tip (black) is set to a potential of 1 V with a ground defined very far away. (b) Dark blue to light blue: Calculated coupling g with the force stemming from the tip voltage and 500 elementary charges at $r = (0, 200, 400, 600, 800, 1000)$nm. Red: Measured g with a parametric drive of $V_{\mathrm{AC}} = 1\,\mathrm{V}$. Dashed black line: Fit of the measured data using 10 charged spots. (c) Distribution of roughly 540 elementary charges leading to the fit in (b).

the position indication in the following. The corresponding spring constant k_{el} gives rise to a frequency shift of both membrane modes, and corresponds to a time-dependent (parametric) coupling J with amplitude $2\omega_0 g$ [5] as

$$\frac{k_{\mathrm{el}}}{m} = -\frac{1}{m}\frac{\delta F_{\mathrm{el}}(t)}{\delta z} = -\frac{q_{\mathrm{surf}}}{m}\frac{\delta E_z(t)}{\delta z} = J(t) = 2\omega_0 g\cos(2\pi f_p t)\,. \tag{S27}$$

For a quantitative analysis of the electrical interaction, we calculate the electrical field of the tip with a finite-element simulation in COMSOL, see Fig. S4(a). We present the field derivatives $\frac{\delta E_z(t)}{\delta z} \propto g$ at different r in Fig. S4(b).

In order to assess the validity of such a simple model, we compare it to experimental evidence. In the main text in Fig. 4(b), we demonstrate how the parametric coupling strength g changes with tip-surface distance d. As Eq. (4) tells us that $g \propto \frac{Z_S}{Z_A}$, we can use the measured amplitude ratio for a direct comparison with the power laws predicted from our simple model. For $d > 500\,\mathrm{nm}$, the measured g fits well to the functional form of $-\frac{\delta E_z}{\delta z}$ at $r \approx 800\,\mathrm{nm}$, while for $d < 500\,\mathrm{nm}$ it fits better to the case of $r \approx 200\,\mathrm{nm}$. None of the simulated single-charge traces can explain the entire measurement.

We can improve the agreement between simulation and experiment by assuming a more realistic charge distribution. The dashed line in Fig. S4(b) corresponds to a heuristic model of 10 charged spots spread between $r = 0$ and $r = 1000\,\mathrm{nm}$, see Fig. S4(c). The surface angle of the charge locations does not enter our calculation, such that

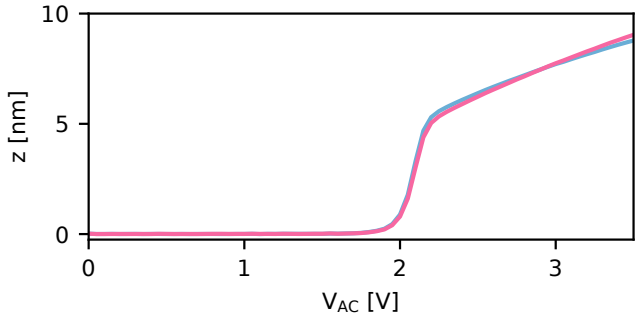

FIG. S5. **Driving at the frequency sum.** Experimental result of driving the two modes at the sum of their frequencies $f_A + f_S$ with a tip-voltage drive and with $d = 1000\,\mathrm{nm}$.

the model is not unique. Nevertheless, the realistic parameters employed, and the excellent agreement with the experimental results in Fig. S4(b) and Fig. 4(b), demonstrate that the surface-charge model can fully explain the parametric coupling observed with out membrane resonators. Unfortunately, the actual charge distribution was not measured with our main device, but the result presented for a second device in Fig. S1 shows a similar spatial distribution as in our calculation, and further supports our claim.

Using the 10 charged spots and the simulated field derivative of the tip, we can numerically calculate the parametric coupling g for any combination of d and V_{AC}. Based on this model, we find the steady-state responses of both modes in Fig. 4(b) with the help of Eq. (2).

S7. DRIVING AT THE FREQUENCY SUM

We also tested parametric driving at the frequency sum $f_\Sigma = f_A + f_S$. Here, owing to the symmetry in the propagation matrix in Eq. (3), the two modes drive each other simultaneously instead of alternatingly. As a result, there is a parametric driving threshold g_{th} where the energy pumped into the system exceeds the energy lost through linear damping [6, 7]. This threshold is reached when the gain factor

$$G = \left[\left(1 + mg\omega_0\sqrt{\frac{Q_S Q_A}{k_S k_A}}\right)\left(1 - mg\omega_0\sqrt{\frac{Q_S Q_A}{k_S k_A}}\right)\right]^{-1} \tag{S28}$$

diverges [6]. With $m = m_A \approx m_S$, $Q_A \approx Q_S$ and $k_A = m\omega_A^2 \approx k_S = m\omega_S^2$, this is the case for $g_{\mathrm{th}} = \Gamma$. With the calibrations from Fig. 3 and 4, we expect this threshold around $V_{AC} = 2.5\,\mathrm{V}$.

In Fig. S5 we observe the amplitude response of the two modes to a parametric sum drive in the absence of an external force. The amplitudes, measured with a narrow-band filter in our lock-in amplifier, remain zero below the threshold at roughly $V_{AC} = 1.8\,\mathrm{V}$. Beyond the threshold, both amplitudes rise quickly and reach a high amplitude limited by the nonlinearity, similar to a parametric oscillator [8]. The difference between the expected threshold ($V_{AC} = 2.5\,\mathrm{V}$) and the measured result could be due to slow drift of the nanopositioner relative to measurements shown in the main text.

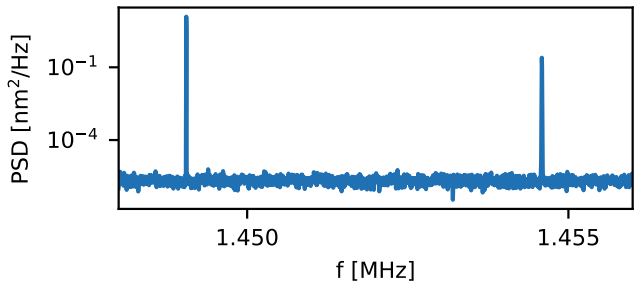

FIG. S6. **Frequency spectrum in the presence of external driving.** In this experiment, the antisymmetric and the symmetric mode were driven by an external laser drive. No side peaks or limit cycles are visible.

S8. SPECTRAL SIGNATURES OF DRIVING

In Fig. S6, we demonstrate that the mode spectrum in the presence of external driving remains very clean. In particular, no evidence of side peaks of limit cycles is observed.

[1] S. M. Yazdanian, J. A. Marohn, and R. F. Loring, Dielectric fluctuations in force microscopy: Noncontact friction and frequency jitter, The Journal of Chemical Physics **128**, 224706 (2008).

[2] J. Moser, A. Eichler, J. Güttinger, M. I. Dykman, and A. Bachtold, Nanotube mechanical resonators with quality factors of up to 5 million, Nature nanotechnology **9**, 1007 (2014).

[3] J. Košata, J. del Pino, T. L. Heugel, and O. Zilberberg, Harmonicbalance.jl: A julia suite for nonlinear dynamics using harmonic balance (2022), arXiv:2202.00571.

[4] L. Papariello, O. Zilberberg, A. Eichler, and R. Chitra, Ultrasensitive hysteretic force sensing with parametric nonlinear oscillators, Phys. Rev. E **94**, 022201 (2016).

[5] M. Frimmer and L. Novotny, The classical bloch equations, Am. J. Phys **82**, 947–954 (2014).

[6] A. Olkhovets, D. W. Carr, J. M. Parpia, and H. G. Craighead, Non-degenerate nanomechanical parametric amplifier, in *Technical Digest. MEMS 2001. 14th IEEE International Conference on Micro Electro Mechanical Systems (Cat. No.01CH37090)* (2001) pp. 298–300.

[7] W. Zhang, R. Baskaran, and K. L. Turner, Effect of cubic nonlinearity on auto-parametrically amplified resonant {MEMS} mass sensor, Sensors and Actuators A: Physical **102**, 139 (2002).

[8] R. Lifshitz and M. C. Cross, Nonlinear dynamics of nanomechanical and micromechanical resonators, in *Reviews of Nonlinear Dynamics and Complexity*, edited by H. G. Schuster (Wiley-VCH Verlag GmbH & Co. KGaA, 2008) p. 1–52.